OBSERVATION STRATEGY FOR OBJECTS ON DECAYING ORBITS

Radu G. Danescu[(1)], Razvan Itu[(1)], Attila Fuzes[(1)], Dan Moldovan[(2)], Vlad Turcu[(2)],

[(1)] Technical University of Cluj-Napoca, Str. Memorandumului 28, Cluj-Napoca, Romania, Email: {radu.danescu, razvan.itu, attila.fuzes}@cs.utcluj.ro
[(2)] Romanian Academy Cluj-Napoca Branch, Astronomical Observatory Cluj-Napoca, Str. Ciresilor 19, Cluj-Napoca, Romania, Email: {dan.moldovan, vladturcu}@acad-cj.ro

ABSTRACT

Space debris in the Low Earth Orbit (LEO) region lose altitude due to friction, eventually undergoing atmospheric re-entry. The predicted position of the object can differ by a significant amount from its true position, and a narrow field of view telescope can completely fail to observe it. We describe a combination between a wide field of view (FoV) instrument and a narrow FoV instrument to observe the object on decaying orbits. The solution includes increasing the sensitivity of the sensors and of the detection algorithms, improving the accuracy of the astrometric calibration without losing real time capabilities, association between the detected tracklets and the predicted positions of the objects, and refinement of orbital parameters for better short and medium term prediction to allow accurate positioning of the telescope.

1 INTRODUCTION

Since the beginning of the space era, the atmospheric re-entries of man-made space objects became an unwanted reality. The international interest towards monitoring re-entry events is growing, taking into account the expanding number of Low Earth Orbit (LEO) satellites launched (LEO large satellites constellations e.g. Starlink, OneWeb, etc.), and the risk associated with reentries of large space debris for human populated areas [1]. Since 1957, the total number of decays recorded in the Space-Track database has reached 117482 [2], and the total number of re-entries (payloads, rocket bodies, debris) from 29 November 2000 up to March 7, 2025 in the CORDS database is 2488 [3]. In order to accurately predict the date and place of the re-entry, accurate observations of the re-entry object must be performed, and complex algorithms have to be employed [4]. Even so, the uncertainties remain large (up to ± 72 hours for 6-7 days before re-entry), due to the unpredictable perturbing forces present in the near-Earth vicinity. The prediction process must take into account complex atmospheric drag models such as the ones described in [5, 6]. The orbital prediction library Orekit [7] implements many of these models, but the models quickly diverge from the real position, and multiple observations must be made to correct them.

As the prediction errors are larger than the field of view of a telescope, wide field of view (FoV) observation systems need to be employed.

The domain of wide FoV surveillance for the LEO objects includes the FireOpal network [8], consisting of multiple all sky observation stations in the Australian desert, the Multi-site All-Sky CameRA (MASCARA) system presented in [9], consists of five cameras with a field of view (FOV) of 53 × 74°, and the LCLEOSEN (Low-Cost Low Earth Orbit optical surveillance SENsor) system presented in [10], consisting of an array of instruments based on wide FOV lenses and CMOS sensor providing full sky coverage. We have also designed a wide FoV surveillance system, based on low-cost components, designed to be easily set up anywhere and to provide real time results [11][12].

However, the wide FoV systems cannot have the accuracy of a narrow FoV system, such as a telescope. While the wider FoV system has a better chance of observing the re-entry object, a telescope's superior angular accuracy allows a better estimation of the object's evolution in time, and therefore for a better prediction of the time and place of contact with the Earth's surface. In a previous work [13], we have proposed a tandem of wide FoV and narrow FoV systems for generic space surveillance in the LEO region, by using very short-term predictions from the wide FoV system results to orient the telescope to the target. In this paper we present the changes that we made to the system in order to adapt it to the more specific and more challenging task of observing re-entry objects, objects having a decaying orbit. We have identified several problems that prevented our previous system to be an efficient tool for observing the decaying orbits, and have proposed solutions for them:

1. The sensitivity of the wide FoV instrument needed to be increased. For that reason, we have switched to using 14 bit RAW files from the DSLR camera, and converted these files to FITS for further processing.
2. The sensitivity of the target detection algorithm from image frames needed to be increased. Our previous work relied on computing differences between frames, but this approach depends on

Proc. 9th European Conference on Space Debris, Bonn, Germany, 1–4 April 2025, published by the ESA Space Debris Office
Editors: S. Lemmens, T. Flohrer & F. Schmitz, (http://conference.sdo.esoc.esa.int, April 2025)

thresholds which, if too low, caused a lot of false positives, especially near the horizon where clouds or city lights can affect the performance. For this reason, we have switched to a machine learning based approach applied directly to the FITS image frames, to identify the candidate regions for streak detection. Once the region was identified, the Hough transform was applied to detect the line segment corresponding to the satellite streak.

3. The wide FoV astrometric calibration's accuracy needed to be improved, especially at the image periphery. For this reason, a tile-based calibration approach was implemented, and the results are fused in a calibration grid that can be used for instant translation between pixel coordinates and equatorial coordinates.
4. Real time recognition of the detected objects is needed, so that we can know which object is the one of interest. We have combined the real time detection process with real time position prediction based on TLE files. The predicted positions are projected in the image space, and can be matched automatically with the detected tracklet based on orientation, tracklet length, and distance between the tracklet and the prediction.
5. The prediction of the object's position in the future, based on the real time results of the wide FoV system needed to be improved to a longer period of time. Therefore, our previous polynomial curve extrapolation of the trajectory was not suitable anymore. We have proposed a solution to quickly adjust orbital parameters based on multiple available TLEs for the reentry object, combined with stochastic diffusion of chosen parameters, to eventually produce a new TLE file with parameters that better fit the current observations. This TLE file can then be used for the prediction of the object in the future.
6. Improved processing of the narrow instrument image sequences: the machine learning based approach for target detection is also applied to the narrow FoV images, improving the results for lower contrast, higher noise, or occlusions such as clouds.

Each of these improvements are described, in more detail, in the following sections.

2 INSTRUMENTS

The measurements are performed using two instruments: a real time, portable, wide field of view (FoV) instrument based on low cost, off the shelf components, and a narrower field of view instrument, based on a refractor telescope and an astronomical camera, deployed at an Astronomical Observatory near the city of Cluj-Napoca.

The wide FOV system uses a Canon EOS 800 D DSLR camera, equipped with a 20 mm focal length Canon EF 20mm f/1.8 USM lens. The image size is set to the maximum 6000x4000 pixels, this being the only resolution available for RAW (uncompressed) output. The 14 bit raw images are converted to 16-bit grayscale FITS images immediately after they are acquired. The camera is synchronized by an external trigger signal based on a GPS receiver, to ensure precise synchronization with the global UTC time. The effective field of view of the system is 60x40 degrees. The control of image acquisition, the target detection, astrometric calibration, and astrometric reduction, .tdm file generation, and orbital parameters refinement is performed in real time on a 13-inch MacBook Pro 2020, equipped with the Apple Silicon M1 processor.

The narrow FOV instrument is equipped with an Orion ShortTube 80 refractor telescope and a SBIG STT 1603ME CCD camera, working in binning mode, producing 16-bit FITS images of 768x512 pixels in size. The telescope is mounted as a secondary telescope on a PlaneWave L600 fast-moving accurate equatorial mount, with an ASCOM compatible software interface, which allows real time orientation towards specified coordinates. The acquisition system is synchronized using a Synoptes precise timestamping device, based on GPS, able to assign microsecond-accurate timestamps to the acquired images [14]. The instrument is placed in the dome of the Feleacu building of the Cluj-Napoca Astronomical Observatory. The images are processed offline, using the same algorithms that are used for the wide FoV instrument.

3 TARGET DETECTION BASED ON NEURAL NETWORKS

Neural networks are widely used for detecting objects of interest from images, if they are properly trained. One of the most popular solutions for is the You Only Look Once (Yolo) network [15]. Several different updates to the original architecture have been released and one of the major milestones came at version number eight, which was released in 2023 [16]. The Yolo framework offers five different model variants where there is a tradeoff between the size of the resulting model, the speed of the detection and the detection performance.

The main challenge was to train the network, because the training process requires a large database of images annotated with the objects of interest (rectangles bounding their position).

3.1 Creating the training dataset

For the purposes of training, we have used images taken by the aforementioned wide FoV system based on Canon EOS camera, at a resolution of 6000 x 4000, raw format,

converted to images of 16 bits pixel depth. To automate the process, we first processed the images using our previous detection algorithms, based on differences between consecutive images. We have selected the detections that lead to formation of tracklets of at least 3 points, as we assumed that these detections had a lower probability of being false positive. These objects formed our initial dataset, which was later verified manually, and all the false positives were excluded.

The large, 6000x4000 pixels images were then split up into smaller tiles of 1000 x 1000 pixels. The result was a total of 1820 annotated images.

The size of the training dataset was then increased by augmentation. This was achieved first by modifying the brightness and contrast values of the images, to simulate fainter streaks or additional light pollution, as seen in Fig. 1.

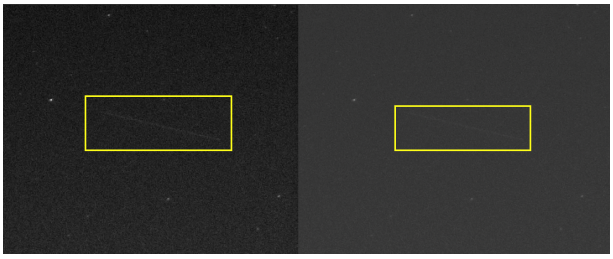

Figure 1. Data augmentation by changing the overall brightness and contrast of the image.

Another method to increase the variability of the dataset and to add more data is to perform rotation and shearing on the images, as shown in Fig. 2. This way, the labelled objects would be at different angles in regard to the ones on the original image, thereby not just increasing the sample size, but also diversifying the data as well.

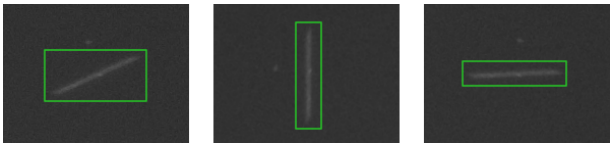

Figure 2. Data augmentation through rotation and shearing.

3.2 Training the network

The augmented image dataset was split into three subsets: 80% of images used for training, 20% for validation and 10% for testing.

For training the network, a workstation with two Nvidia GTX 1080 Ti graphical cards were used.

As the Yolo network's input image size has to be a multiple of 32, we have chosen to set it to 640x640 pixels. The initial tiles of 1000x1000 were scaled down to 640x640 for training and for inference. The pixel values for the network are floating point values ranging from 0 to 1. We took advantage of this fact and scaled the 16-bit to the 0..1 interval, but we could also use, with the same network, 8-bit values from jpeg images, the only change needed being to use a different scale factor.

The smaller image size (640x640 instead of 1000x1000) meant that the training time and inference time were reduced by a factor 1.66 overall, without taking into consideration other parameters.

The training of the individual networks took anywhere between 3 – 8 hours depending on the model variant selected. We have trained the Yolo v8 with different sizes: nano (3 million parameters), medium (26 million parameters), and large (44 million parameters).

3.3 Real time inference

While the training process was implemented in Python, we needed to integrate the inference process in the real time C++ based application.

Since we wanted to perform the inference tasks on an Apple MacBook Pro with using Apple's own Metal Performance Shader (MPS) graphical acceleration back-end, we converted the trained model to an MPS-compatible TorchScript format. The main application is designed to be able to load different models without changing the source code. Therefore, we could load nano, medium or large Yolo models, or models trained using different settings or data sets. The models can differ in size, but they must obey the input and output formats.

For the real-time inference process, we use the same trained model for all types of images:

- For 6000x4000 images, we split the image in overlapping tiles of 1000x1000, with a stride of 500 pixels on both axes. The tiles are then scaled to 640x640 pixels and fed to the model for prediction of the object bounding rectangles. The results are then fused: if some rectangles are overlapping, a larger rectangle to include them is generated.
- For the narrow FoV instrument, generating 768x512 pixels images, the images are scaled to 640x640 pixels and fed to the model for prediction.

Due to the fact that the large FoV images require multiple prediction from the trained model, and also that the large FoV images have to be processed in real time, the model of choice was, eventually, the Yolo nano. With this model we could complete the whole processing cycle in less than 5 seconds on the 2020 MacBook Pro (M1). However, the application framework allows us to change to a larger model when we switch to a more powerful computer.

After the Yolo-based prediction, we need to find the

streak as a line segment. We perform the following steps for each rectangle:

- Adaptive thresholding of the original grayscale image for the region of interest described by the predicted rectangle (if more rectangles are overlapping, which may be the case for the wide FoV system, as we use overlapping tiles for prediction, the rectangles are fused into a larger rectangle).
- Use of the Probabilistic Hough Transform of OpenCV to detect line segments inside the region of interest.
- If more than one line segment is detected inside the region, the longest segment is kept as the streak result.

The process is depicted in Fig. 3.

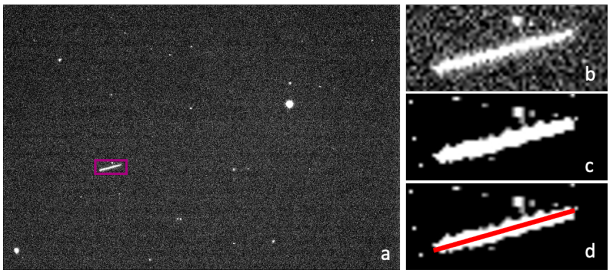

Figure 3. Post-processing of the neural network based predictions to obtain the satellite streak line segments: a – the Yolo-based detection, b – highlight of the detection region, c – binarization, d – Hough transform based line segment detection.

4 REAL TIME ASTROMETRIC CALIBRATION

The detection results, in pixel coordinates, are only useful if they can be converted in equatorial coordinates as soon as possible, so that they can be used to refine the orbital parameters of the target. The astrometry tools available from astrometry.net [17] can be used to calibrate any image that contains a star field, and then to map the image pixel coordinates to equatorial coordinates. A wide field of view (60x40 degrees) poses some challenges to the astrometry tools, especially for peripherical image areas. For this reason, and also for real time performance, we have proposed, in a previous work [12], a grid-based accumulation of calibration results, so that the errors can be filtered using multiple calibrations, and the pixel space to equatorial coordinates conversion can be achieved in real time.

In order to further increase the accuracy in the peripheral regions of the image we took the grid approach one step further and used a tile-based calibration approach. Instead of only performing calibration on the whole image, we also performed calibration on image quarters, and then combined all results in the same calibration grid.

The calibration result on the whole image is shown in Fig. 4. We can see the recognized stars and constellations. At a first glance, the calibration process was accurate and the catalogue stars are matching the stars in the image. However, when zooming in on the image corners, as shown in Fig. 5, we can see that the peripheral stars do not match with the image. If we pass to the astrometry engine only the top left quarter of the image, the results improve significantly, as shown in Fig. 6. In this figure, which shows again a zoomed in detail of the top left corner, we can see that the catalogue stars are now well aligned with their position in the image.

The quarter based (tile-based calibration) does not impede the real time behaviour of the system. It is executed in a background process and updates the grid when possible, but the grid is also usable from the moment the first full frame calibration is completed. Thus, the system is able to quickly produce equatorial coordinates, but as the time goes by, the accuracy of the angular coordinates increases as the grid is updated with more accurate, tile-based calibration data results.

Figure 4. Full field calibration results, showing the identified constellations.

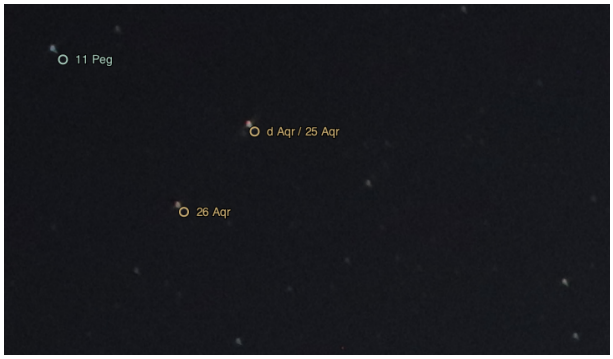

Figure 5. Full field calibration results, zoomed in detail showing that peripheral stars in the top left corner are not properly matched by the calibrated model.

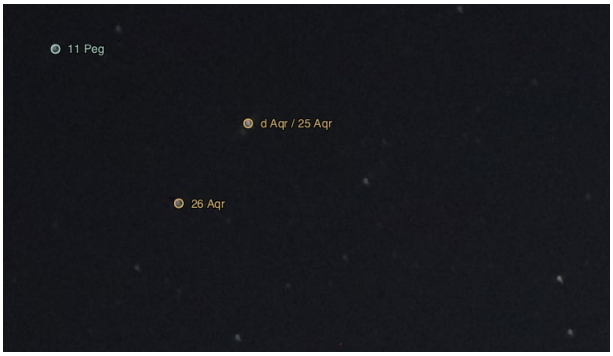

Figure 6. Quarter field calibration results, zoomed in detail showing that peripheral stars in the top left corner are properly matched by the calibrated model.

5 REAL TIME TARGET RECOGNITION

Due to the vast quantity of satellites in the low Earth orbit, it is important to recognize if the detected tracklets are of interest or not. We have implemented a method for generating real time predictions, projected in the image space, based on a file of TLE lines, such as the ones that can be downloaded from space-track.org. In order to achieve real time performance, the algorithm relies on the following steps:

1. Generating predictions for every satellite in the TLE file, at every 60 seconds, for the projected duration of the observation session (usually not more than 1 hour). This computationally expensive step is achieved using Orekit and will not affect the real time performance of the system, as it is done before the actual detection process.
2. During detection, identify the satellites that are in the field of view of the system at a given time, by computing the angular distance between 60 second trajectory endpoints and the image centre and image corners.
3. For the identified objects, use linear interpolation based on the current UTC time stamp to compute an approximate position for the exact time. By using linear interpolation of the trajectory, we avoid computing the position of the satellites for every second.
4. The trajectories and the current predicted position are displayed on the original acquired image.
5. If currently detected tracklets match the predicted trajectories, a preliminary automated recognition of the object is achieved.

More details about the automatic association between detected tracklets and the predicted satellite positions can be found in [18].

The result of automatic object identification is shown in Fig. 7. The detected tracklets are shown in color, and the predicted trajectories are shown as white lines. A recognized trajectory, associated with a tracklet, is shown as a thick white line. A cross sign marks the current predicted position of the satellite.

Figure 7. Real time prediction of satellite trajectories and automatic recognition of detected tracklets

For observing the decaying orbits of re-entry bound objects, the automatic recognition system is adapted so that it will use only the TLEs of the objects of interest. The TLE file used as input will contain more than one version of the orbital parameters, because these parameters change rapidly, and the best prediction of the object's position is not always generated by the latest set.

Sometimes the predicted trajectory is not close enough to the actual position of the object to be recognized automatically. In this case we have provided a manual override. The user sees, in real time, the evolution of the predicted position and the evolution of the detected position and can use the application interface to select the tracklet and force association. Such a case is shown in the results chapter of this paper, caused by a combination of out-of-date TLEs and a highly eccentric and rapidly decaying orbit.

6 ORBITAL PARAMETERS REFINEMENT

Once the object is detected and a TDM file is generated, the orbital parameters refinement process can be applied. The general idea is to adjust the parameters to match the measurement data, so that these parameters will produce better predictions in the (near) future, and these predictions can position a narrow field instrument more accurately.

From analysing the historical TLE files of re-entry bound objects, we could see that the most unstable orbital parameters were the Right Ascension of the Ascending Node, the Argument of Perigee, and the Mean Anomaly (which is correlated with the Argument of Perigee). The most stable parameters are the Inclination, and the Mean Motion, but they can also start to change rapidly when the orbit is severely decaying. Our purpose is not to follow a classical Orbit Determination procedure, which

accurately produce correct orbital elements, but to generate elements that can produce better predictions for the next minutes or tens of minutes, so that a narrower FoV instrument can better observe the object. For this reason, we have chosen to alter only two parameters: the Right Ascension of the Ascending Node and the Argument of Perigee, and we assume that all the other parameters remain fixed.

Our initial approach was based on the Extended Kalman Filter (EKF), an estimator which adjusts the model parameters based on measurements in a single step, based on the assumed covariance of the parameters and a local linearization of the mapping between the model parameters and the measurement space. This approach is suitable for minor differences between prediction and measurement but proved to be unsuccessful for more severe orbital decay, such as the one we present in the results section. Faced with this situation, we have changed the approach towards a stochastic approach. The idea is underlined in Fig. 8. The steps of the algorithm are the following:

1. Starting from an input file containing *N* TLEs for the target object, we generate *N*S* hypotheses by randomly altering the Right Ascension of the Ascending Node and the Argument of Perigee parameters with random amounts, positive or negative, in a specified range. *S* is a parameter of the algorithm, describing the number of random samples to be extracted for each given TLE. We'll call this step *Stochastic Diffusion*.
2. Using the Orekit library and the timestamps from the measurement TDM, we generate measurement predictions for all the parameter sets produced by the stochastic diffusion.
3. The predictions are compared, point by point, with the actual measurement, and a mean angular distance is computed for each prediction.
4. The predictions are sorted by their distance to the measurement, and the best *M* sets are kept.

The steps from 1 to 4 are repeated multiple times (we currently repeat four times), gradually decreasing the range for the stochastic diffusion, the number of steps *S* and the number of accepted best sets *M*. For the last step, *M* is set to 1, meaning that a single TLE set is generated.

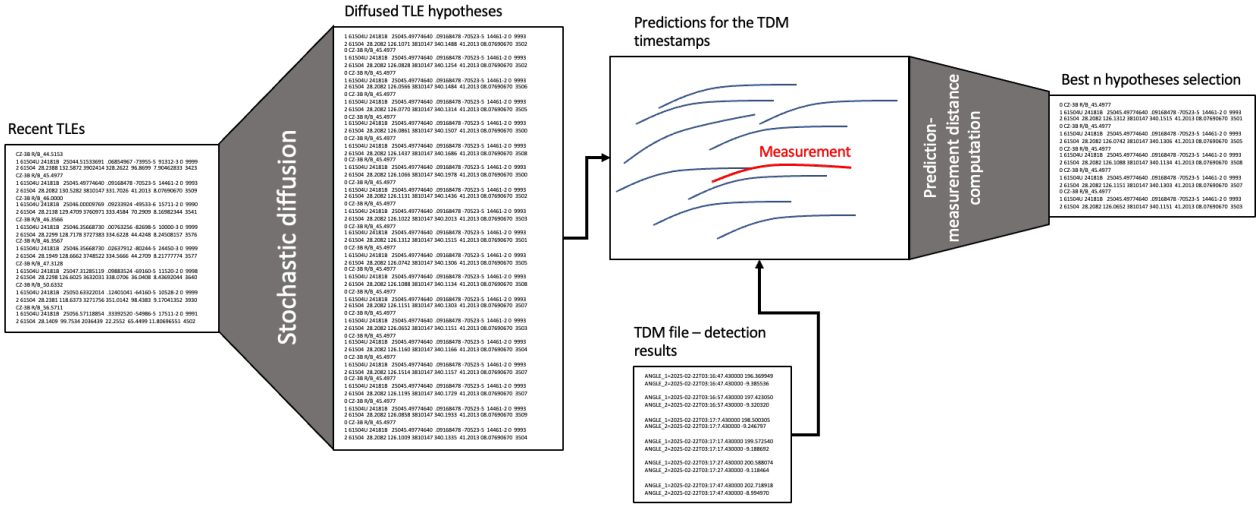

Figure 8. The stochastic method of orbital parameters refinement

7 TESTS AND RESULTS

We have attempted to observe the re-entry process of the CZ-3B R/B rocket body (NORAD ID 61504), an object on a rapidly decaying eccentric orbit. Our first successful attempt was made on the early morning of February 22, 2025. At that time, the latest available orbital parameters downloaded from space-track.org were generated on February 19, 2025.

We observed the object with the wide field of view system two times, the first time from UTC 3:16:47 to UTC 03:17:47 (6 frames taken at 10 seconds apart), and the second time from UTC 3:20:6 to 3:22:4 (12 frames, but the object was not detected in every frame). The urban location of the wide FoV system and the low altitude of the object made the detection difficult. A sample frame from the sequence is shown in Fig. 9, and a detail of the object in a selected region of interest is shown in Fig. 10.

Figure 9. Large FoV image acquired from an urban location (contrast enhanced).

Figure 10. Detail showing the observed object (35 pixels wide, in a 6000x4000 pixels image)

The main challenge was, however, the highly outdated set of orbital parameters. During the automatic detection process we have projected, in real time, the predicted position from 8 available parameter sets, the oldest being from February 13 and the newest from February 19, 2025. To our surprise, the best match between the prediction and the detection was not for the newest parameter set, but for the one generated on February 14. Even so, the angular distance between predicted and measured equatorial coordinates was more than 10 degrees. The main problem was that the error was not only along the track, meaning that a narrow field telescope would eventually observe it with some delay, but it also had more than 3 degrees of cross track error, which was more than the angular field of view of the narrow instrument, as shown in Fig. 11.

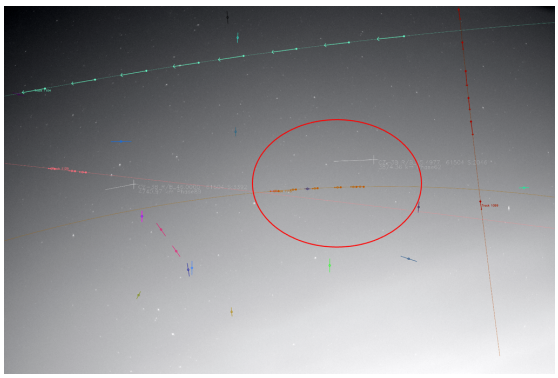

Figure 11. Detected object compared with the predicted position (white line and cross), highlighted

We have applied the orbital parameter refinement algorithm based on Monte Carlo sampling and testing, using the first detection results as input. We have obtained refined orbital parameters and the average angular error for the first sequence was reduced to less than 0.1 degrees. Using the refined parameters, we have compared the predicted positions for the second sequence with their corresponding measured positions. While the predictions were not perfect, the errors were greatly reduced to an average of 0.5 degrees, with a less than 0.3 degrees cross track error, meaning that the object would be easily observed by a narrow field of view instrument oriented towards the predicted position. The process is depicted in Fig. 12. The time between the two sequences is about 2 minutes, which is more than enough for the execution of the refinement algorithm and for commanding the orientation of other instruments.

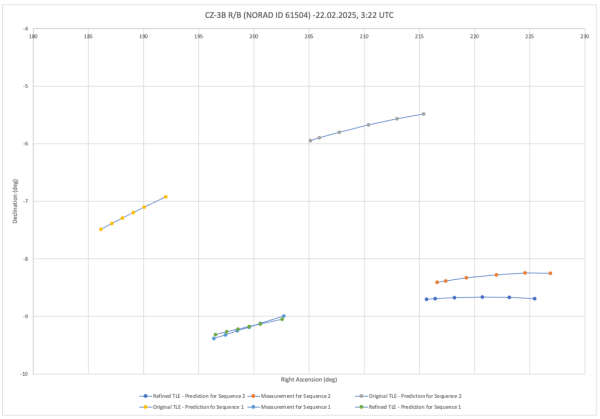

Figure 12. Comparison between predicted positions and measured positions, for two sequences, large FoV instrument, February 22.

The second test was performed on February 26, 2025, from UTC 3:46 to UTC 3:55, using the narrow field of view system. This time, the most recent TLE parameters were generated on February 25, at 13:42 UTC, so they were fairly recent. Based on these parameters, the object's position was predicted accurately enough that the narrow field instrument was properly positioned. The object was observed in 15 sequences, each sequence was obtained in sidereal tracking mode, corresponding to a fixed telescope position in equatorial coordinates. A sample image, showing the object's position at UTC 3:47:02, is shown in Fig. 13.

Figure 13. Sample image from the narrow FoV instrument (contrast enhanced), showing the observed object

The first sequence was processed automatically to generate the tracklet TDM. The detected positions in the image space are shown in Fig. 14. The object was not detected in all the frames, due to its rapid spinning which caused a large variability of its brightness. The first detected sequence was compared to the available TLEs and, through the stochastic refinement process, produced a refined TLE for better prediction of the next positions. The initial average error was 2.5 degrees, mostly along track, meaning that the prediction was good enough for the narrow FoV instrument positioning.

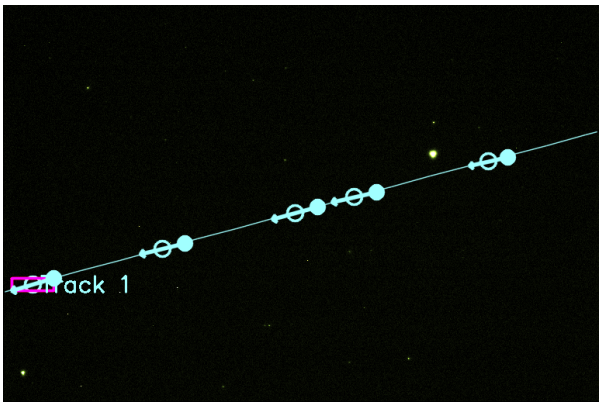

Figure 14. Result tracklet for the first sequence of the narrow instrument

We have used the results of the first sequence to refine the orbital parameters, and after this process the predictions for the first sequence matched the measurement perfectly, as shown in Fig. 15. However, in order to test the usefulness of the refined parameters we used them to generate predictions for the last sequence, 7 minutes later. For this sequence the predictions based on the initial TLE had an angular difference of 1.5 degrees from the measured positions. The refined parameters reduced this error to about 0.5 degrees. The process is shown in Fig. 15: the initial sequence is shown in the top left corner, and the last sequence in the bottom right corner.

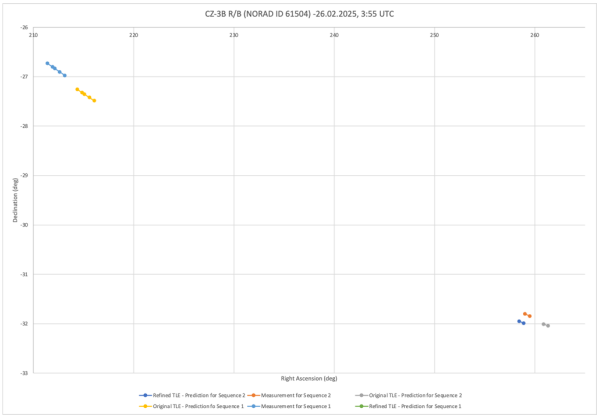

Figure 15. Comparison between predicted positions and measured positions, for two sequences, narrow FoV instrument, February 26

The object is no longer in orbit. It has re-entered the atmosphere on February 28, 2025 [3].

8 CONCLUSION

Observing the objects on decaying orbits, destined for re-entry, is a challenging task, especially due to the rapid change between the actual orbit and the one modelled by the known parameters. Our proposed solution is a combination of a wide FoV instrument for acquiring the target, and a narrow FoV instrument for precise measurement of its position. Our contribution includes a generic, machine learning based target detection solution that can be applied to any type of image, taken from both the narrow FoV and the wide FoV sensors, on any bit depth, the automatic association of the detected tracklet with the predicted position from known orbital parameters, and the generation of new, updated orbital parameters based on stochastic filtering. Future work will be focused on the full automation/robotization of the process.

9 ACKNOWLEDGMENT

The research was supported by a grant from the Ministry of Research, Innovation and Digitization, CNCS/CCDI–UEFISCDI, project number PN-IV-P6-6.3-SOL-2024-2-0220, within PNCDI IV.

We dedicate this work to the memory of Octavian Cristea (1956-2025), our partner in many space-related research projects, who inspired our first steps in surveying the LEO region.

10 REFERENCES

1. Federal Aviation Administration (2023). Risk Associated with Reentry Disposal of Satellites from Proposed Large Constellations in Low Earth Orbit.

URL: https://www.faa.gov/sites/faa.gov/files/Report_to_Congress_Reentry_Disposal_of_Satellites.pdf, Accessed: March 7, 2025.

2. Space Track (2025). Space Track Decay Data. URL: https://www.space-track.org/#decay (required login), Accessed: March 7, 2025.

3. Aerospace Corporation (2025). The CORDS reentry database. URL: https://aerospace.org/reentries, Accessed: March 7, 2025.

4. European Space Agency (2025). Reentry and collision avoidance. URL: https://www.esa.int/Space_Safety/Space_Debris/Reentry_and_collision_avoidance, Accessed March 7, 2025.

5. Picone, J.M., Hedin, A.E., Drob, D.P. & Aikin, A. C. (2002). NRLMSISE-00 empirical model of the atmosphere: Statistical comparisons and scientific issues. *Journal of Geophysical Research* **107** (A12), 1468.

6. Bowman, B.R.,Tobiska, W.K., Marcos, F.A., Huang, C.Y., Lin, C.S. & Burke, W.J. (2008). A New Empirical Thermospheric Density Model JB2008 Using New Solar and Geomagnetic Indices, In *Proc. AIAA/AAS Astrodynamics Specialist Conference*, American Institute of Aeronautics and Astronautics, 6438.

7. Orekit (2025). Orekit - An accurate and efficient core layer for space flight dynamics applications. URL: www.orekit.org, Accessed: March 7, 2025.

8. Bland, P., Madsen, G., Bold, M., Howie, R., Hartig, B., Jansen-Sturgeon, T., Mason, J., McCormack, D. &, Drury, R. (2018). FireOPAL: Toward a Low-Cost, Global, Coordinated Network of Optical Sensors for SSA. *In: Proc. of the 19th AMOS (Advanced Maui Optical and Space Surveillance Technology Conference)*, Wailea, Maui, Hawaii, USA, Sept. 5–18.

9. Wijnen, T.P.G., Stuik, R., Redenhuis, M., Langbroek, M. & Wijnja, P. (2019). Using All-Sky optical observations for automated orbit determination and prediction for satellites in Low Earth Orbit. In *Proc. of the 1st NEO and Debris Detection Conference*, Darmstadt, Germany, 22–24 January 2019, 1–7.

10. Kerr, E., Normen, J., Sahcnez Ortiz, N., Del Campo, B., Maric, N., Falco, G., Dorn, C. & Eves, S. (2021). Design and prototyping of a low-cost LEO optical surveillance sensor. *In Proc. of the 8th European Conference on Space Debris*, Darmstadt, Germany, 20-23 March 2021.

11. Danescu, R., Itu, R., Muresan, M. P., Rednic, A. & Turcu, V. (2022). SST Anywhere-A Portable Solution for Wide Field Low Earth Orbit Surveillance. *Remote Sensing* **14**(8), A1905.

12. Danescu, R., Itu, R., Fuzes, A. & Turcu, V. (2024). Increasing the accuracy of real time wide field of view space surveillance by grid-based combination of multiple calibration results. *Advances in Space Research* **73**(3), 2098-2118.

13. Danescu, R.G., Itu, R., Turcu, V.S. & Moldovan, D. (2023). Adding Surveillance Capabilities to a LEO Tracker Using a Low-Cost Wide Field of View Detection System. In proc: *2nd NEO and Debris Detection Conference*, Vol 2, 24- 26 January 2023, Darmstadt, Germany, published by ESA Space Debris Office, 1-11.

14. Balan, M., Apostol, A.R., Cherciu, C., Turcu, V., Nedelcu, A., Trelia, M.M. & Mihai, S.S. (2022). Synoptes – Precise GNSS Timestamping Device for Space Surveillance and Tracking Operations. In Proc: *73rd International Astronautical Congress 2022, 20th IAA Symposium on Space Debris* (A6), Paris, France. Paper ID: 68551.

15. Redmon, J., Divvala, S., Girshick, R. & Farhadi, A. (2016). You Only Look Once: Unified, Real-Time Object Detection. In Proc. *2016 IEEE Conference on Computer Vision and Pattern Recognition (CVPR)*, Las Vegas, NV, USA, 779-788.

16. Varghese, R. & Sambath, M. (2024). YOLOv8: A Novel Object Detection Algorithm with Enhanced Performance and Robustness. In Proc. *2024 International Conference on Advances in Data Engineering and Intelligent Computing Systems (ADICS)*, Chennai, India.

17. Lang, D., Hogg, D. W., Mierle, K., Blanton, M., & Roweis, S. (2010). Astrometry.net: Blind astrometric calibration of arbitrary astronomical images. *The Astronomical Journal* **139**(5), 1782–1800.

18. Danescu R., Fuzes A., Itu R., Turcu V. (2023). Real Time Orbital Object Recognition for Optical Space Surveillance Applications. *Proceedings of the International Conference on Informatics in Control, Automation and Robotics*, Rome, Italy, November 13-15, Volume 1, pp. 562 – 569.